THE FLARES OF APRIL 1980

A Case for Flares Caused by Interacting Field Structures

MARCOS E. MACHADO
Observatorio de Física Cósmica – CNIE, 1663 San Miguel, Argentina
BORIS V. SOMOV
P.N. Lebedev Physical Institute, Moscow, U.S.S.R.
MARTA G. ROVIRA
I.A.F.E., Buenos Aires, Argentina
and
CORNELIS DE JAGER
Space Research Laboratory, Utrecht, The Netherlands

(Received 24 September, 1982)

Abstract. We discuss the spatial and temporal characteristics of X-ray flares occurring in the active region NOAA 2372 from April 6 to 13, 1980. The flares are seen to extend in most cases across the whole active complex, involving several magnetic features. They originate in an intermediate bipole, between the two main sunspots of the active region, where high magnetic shear was detected. A rapid expansion is seen in some cases, in conjunction with the start of the impulsive hard X-ray bursts. We also detect, in the late phases of some of the events, a large soft X-ray structure overlying the whole active region, which also shows up as a noise storm region at metric wavelengths. These large loops cool by heat conduction but, in some cases, Hα condensations seem to appear, probably as a result of magnetic compression and a condensation mode of the thermal instability. The topological aspects of the field configuration are discussed, in the context of flare models invoking magnetic reconnection at the site of the primary energy release. In such a model, the intermediate bipole is the natural site of initial magnetic reconnection, particle acceleration and heating. In one particular case of a flare observed at the limb, we find possible evidence of particle acceleration in a neutral sheet at the boundary between two clearly defined magnetic structures.

1. Introduction

The active region (AR) NOAA 2372 was observed by the pointed instruments on the Solar Maximum Mission (SMM) spacecraft from the late hours of April 6, 1980 through April 13, when it disappeared beyond the western limb.

During this period it produced a large quantity of flares (more than 50 according to ground based observatory reports) of diverse importance both in Hα and soft X-rays.

High quality magnetic field data were obtained at the Marshall Space Flight Center (MSFC), where both longitudinal and transverse components of the field were measured. Krall *et al.* (1982) give a detailed account of the time development of vector magnetic fields from April 5 to 7.

In this paper we discuss the observations obtained by the Hard X-Ray Imaging Spectrometer (HXIS, van Beek *et al.*, 1980) of six of the best observed X-ray flares. We

Solar Physics **85** (1983) 157–184. 0038–0938/83/0851–0157$04.20.

describe their spatial and temporal evolution and particular features of their high energy photon emission ($E \leq 30$ keV). We relate these observations to the magnetic field data and the characteristics of the radio bursts associated with the flares, as well as Hα structural details. We end our discussion by proposing a topological approach to be developed in order to understand the basic processes leading to flare production.

2. Instrumental Capabilities

The HXIS is able to image solar X-ray emission in six energy bands within the energy range between 3.5 to 30.0 keV, with a spatial resolution of 8″ (FWHM) in its fine field of view (∅ 2′40″) and 32″ over a much larger area (∅ 6′24″) in its coarse field of view.

The six energy bands (B1 to B6) are split in the following way: B1: 3.5 to 5.5 keV; B2: 5.5 to 8.0 keV; B3: 8.0 to 11.5 keV; B4: 11.5 to 16.0 keV; 16.0 to 22.0 keV; and B6: 22.0 to 30.0 keV. Temperatures and emission measures, as well as power law indices can be determined through measured count rates using a count rate prediction program (CRPP, see van Beek *et al.*, 1981) that folds an assumed flare spectrum through HXIS and predicts the count rates in each band.

As mentioned by van Beek *et al.* (1980) in the high temporal resolution mode of operations (typically 1.5 s) only a fraction of the fields of view (15% of the fine and 25% of the coarse in the default mode) data are transmitted. The selection of image elements is based on their brightness, starting with the brightest group of four pixels in the 3.5 to 5.5 keV range. It is thus evident that data on large faint features will not be seen in the transmitted images during the period of the high temporal resolution mode. In the low resolution mode (typically 4.5 s) a much larger fraction (≥ 60%) of the fields of view is transmitted, and during the 'quiet' mode (7 s) all pixels of both fine and coarse are transmitted.

High energy 16 to 22 and 22 to 30 keV X-rays are also recorded by the HXIS high energy monitor (HEM) without spatial resolution but with high sensitivity.

3. Characteristics of the Active Region

Active region 2372 was born on April 4, 1980 in the N–E quadrant of the disk. It was characterized by the presence of two large sunspots of opposite polarity and a small bipolar group located between the two main spots. The resulting polarity structure was thus of the minus-plus-minus-plus type, as shown in Figure 1a.

The region underwent rapid development, its most striking characteristic being that the small bipolar region located between the main spots migrated from the trailing to the leading portion of the region. Significant motions occurred only from April 5 to 7, showing the negative (trailer) polarity spot moving towards the east and the intermediate bipole coming closer to the leader. According to Krall *et al.* (1982), by $14^{h}06^{m}$ on April 7 the motions ceased and no measurable changes were observed later on.

Through much of the time while the region developed the intermediate bipolar structure showed evidences of high magnetic shear, as evidence by measured transverse

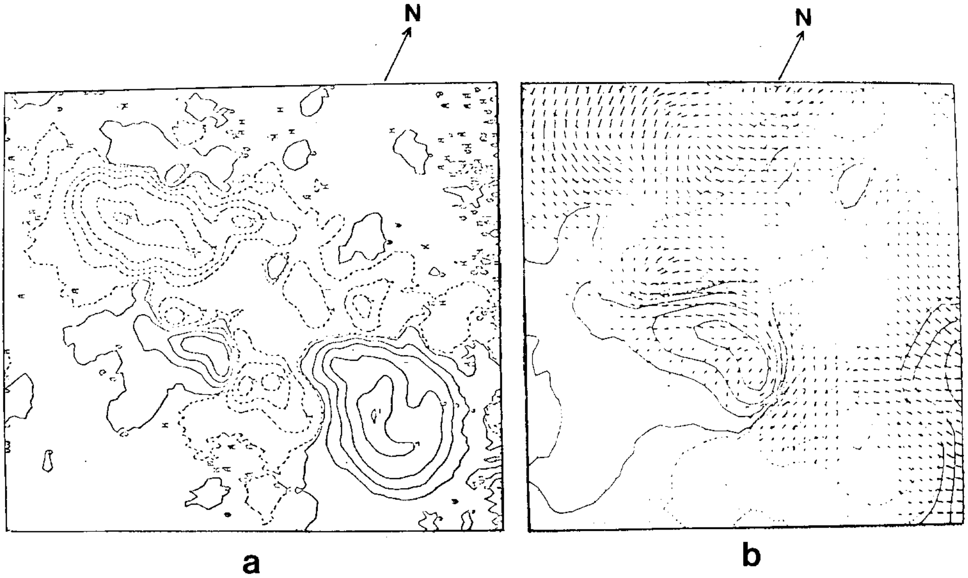

Fig. 1. Overall longitudinal magnetic field configuration of AR 2372 (a) and blow up of the intermediate bipolar region, where both longitudinal and transverse field components are shown (b). Note the high magnetic shear in (b), as evidenced by transverse field components running parallel to the neutral line. (Courtesy of J. B. Smith, Jr., MSFC.)

field components running parallel to the neutral line of longitudinal field. Figure 1b shows clear example of such a situation. It has also been possible to observe other regions of less pronounced shear, being located in the proximity of either the leading or trailing spot. We shall refer to these observations when appropriate for our discussion.

4. X-Ray Observations

We selected six flares (Table I) for detailed study of their X-ray characteristics. Although this is a small fraction of the total, these events show most of the general characteristics

TABLE I

List of events studied in this paper

Date	Hα (beg. – max – end UT)	Hα importance	X-ray class	Position
7 April	B 00:51 – 01:07 – 02:06	1B	M4	N 10 E 03
7 April	05:18 – 05:38 – 06:20	1B	M8	N 12 E 01
8 April	03:03 – 03:10 – 03:50	1B	M4	N 12 W 10
10 April	09:14 – 09:23 – 09:45	1N	M4	N 12 W 42
13 April	04:05 – 04:15 –A 04:17	1F	M1	N 10 W 77[a]
13 April	B 08:40 – 08:40 –A 08:45	–N	C6	N 11 W 80

[a] In the flare Hα reports another event is listed, starting at $04^{h}10^{m}$ and located at N 10 W 85. We conclude (cf. Section 4.4.) that this chromospheric brightening is associated with the energization of a large loop structure directly linked with the same flare.

of the flares produced by AR2372, and are, in their major part, the largest events observed by the SMM experiments. We proceed now to a general description of each of the events, starting with the one on April 8 which was well observed by all the SMM instruments (see e.g. Cheng *et al.*, 1982).

4.1. APRIL 8, 03^h03^m UT

In Figure 2 we show the temporal development of the spatial structures as seen in the HXIS softer energy band (B1: 3.5–5.5 keV), together with a sketch of the magnetic configuration as deduced from the MSFC magnetograms. The alignment of the X-ray and magnetic features was done through the use of an Ultraviolet Spectrometer and

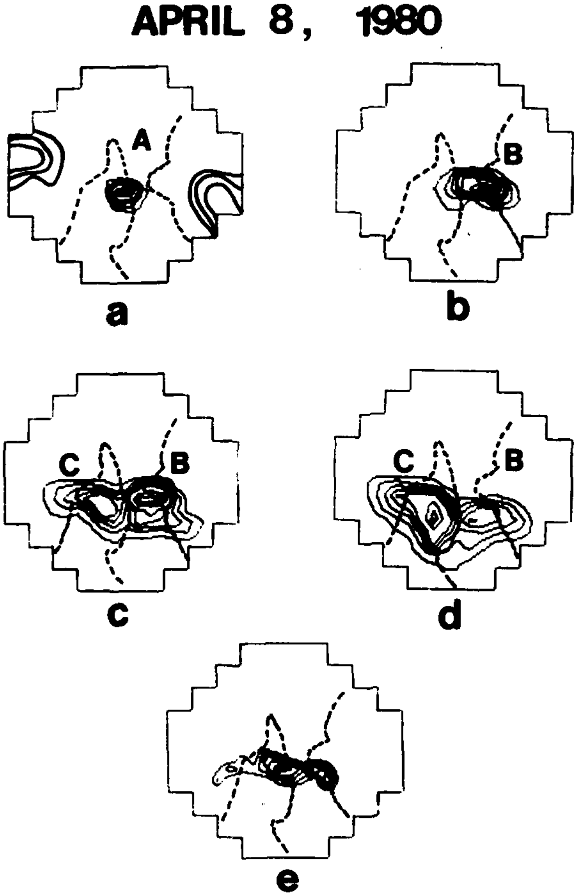

Fig. 2. Soft X-ray (3.5 to 5.5 keV) contour maps (a–d) at different times during the development of the April 8, 1980 flare. The three different soft X-ray structures discussed in the text are indicated, as well as the sunspots (2a) and neutral lines. Soft X-ray contour levels correspond to 10, 20, 30, 40, 50, 75, 90, and 99% of the maximum in this and, unless otherwise indicated, in the subsequent figures. The times correspond to: (a) 03:01:50 UT, (b) 03:05:39 UT, (c) 03:10:43 UT, and (b) 03:16:42 UT. Figure 2e shows harder (11.5 to 30.0 keV) emission at the time of the impulsive burst in the hard X-rays (03:04:07 UT).

Polarimeter (UVSP, Woodgate *et al.*, 1980) raster in a way similar to that described by Duijveman *et al.* (1982).

At around 03^h02^m UT the initial soft X-ray brightening occurs above the intermediate bipolar region of highly sheared field configuration (Figure 2a, feature A). Weak hard X-ray emission (22.0–30.0 keV) is recorded by the HXIS high energy monitor, but it is not locatable in the fine field of view images. In the 11.5 to 16.0 keV images the emission is observed to be co-spatial with that at lower energies, i.e. concentrated within feature A.

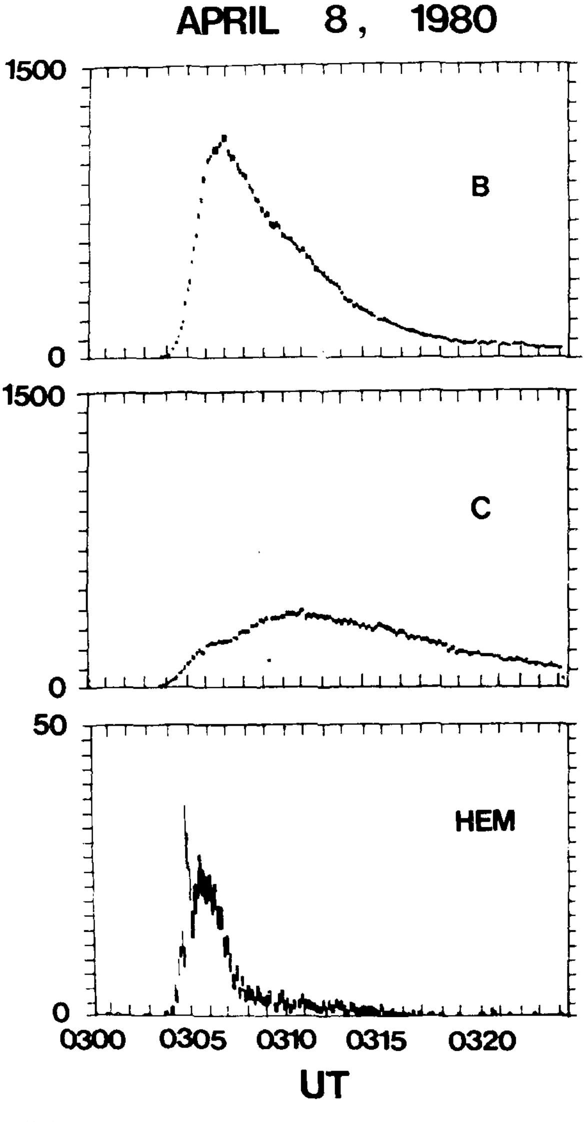

Fig. 3. Soft X-ray (3.5 to 8.0 keV) emission light curves (in counts s^{-1}) of features **B** and **C** in the April 8 flare, and High Energy Monitor (HEM) 22.0 to 30.0 records, showing the two components of the hard X-ray burst discussed in the text.

At the start of the impulsive hard X-ray peak the structural details, both in soft and hard X-rays, change. A strong brightening is observed in the soft X-rays along a feature (**B**) connecting the bipolar region and the leader spot (Figure 2b), while two bright regions appear in the harder X-ray recors (11.5–30.0 keV) at both extremes of the soft X-ray patch (Figure 2e). This behavior is typical of flares showing high energy footpoints due to thick target bremsstrahlung by accelerated particles (Duijveman *et al.*, 1982; Hoyng *et al.*, 1981a; Machado *et al.*, 1982). The location of these two high energy patches coincides with the position of the feet of an active region loop observed by the UVSP (Cheng *et al.*, 1982).

Simultaneously to this happening, a third structure (**C**) located between the bipolar region and the trailer starts to brighten. This structure is clearly visible in the 03^h10^m UT contour diagram of Figure 2c, when its brightness has become comparable to that of structure **B**. Figure 3 shows the 3.5 to 8.0 keV light curves of structures **B** and **C**. Feature **A** contributes about equally in the two plots to the intensity recorded before the impulsive hard X-ray burst.

The gradual hard X-ray component, seen in the 22.0 to 30.0 keV light curve of Figure 3c, originates throughout all its lifetime from within structure **B**, as shown in Figure 4. There are no evidences of footpoint structures, as those seen at the time of the impulsive peak, during this period. During this gradual period, the brightest spot in the hard X-rays is clearly embedded within the soft X-ray patch, suggesting, as discussed by Hoyng *et al.* (1981a) and Machado *et al.* (1982) the existence of high temperature thermal regions of a small size. A two-temperature analysis of the 3.5 to 30.0 keV emission during the lifetime of the gradual burst indicates the presence of $6 \times 10^7\,\mathrm{K} \leq T \leq 9 \times 10^7\,\mathrm{K}$ components with emission measures $10^{47}\,\mathrm{cm}^{-3} \leq EM \leq 4 \times 10^{46}\,\mathrm{cm}^{-3}$, superimposed over the $\approx 2 \times 10^7$ K emission of the

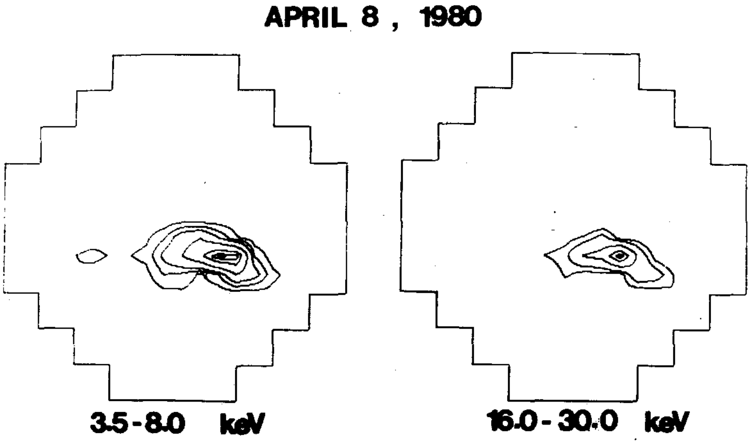

Fig. 4. Soft and hard X-ray emission contours obtained through a 16.5 s integration period at 03 : 05 : 02 UT, during the gradual component of the hard X-ray burst (cf. Figure 3). Note the single source appearance in the harder X-ray records. Emission contours in the 16.0 to 30.0 keV range correspond to 20, 30, 50, 75, and 90% of the maximum. In the lower percent levels considerable counting rate due to the soft X-ray emitting plasma is present.

softer X-ray component. It has been shown by Machado *et al.* (1983) that the existence of these high temperature components implies quasi-continuous energy release within the loop structures. One obtains a similar conclusion from the analysis of high resolution (≈ 1 keV) observations in the energy range 13 to 300 keV of Lin *et al.* (1981).

In Figure 5 we have plotted the soft X-ray temperature and emission measure values obtained for features **A**, **B**, and **C**. Before the start of the impulsive burst mostly feature **A** contributes to the total X-ray output, while immediately after, feature **B** shows a steep increase both in T and EM, continuing over the lifetime of the gradual hard X-rays.

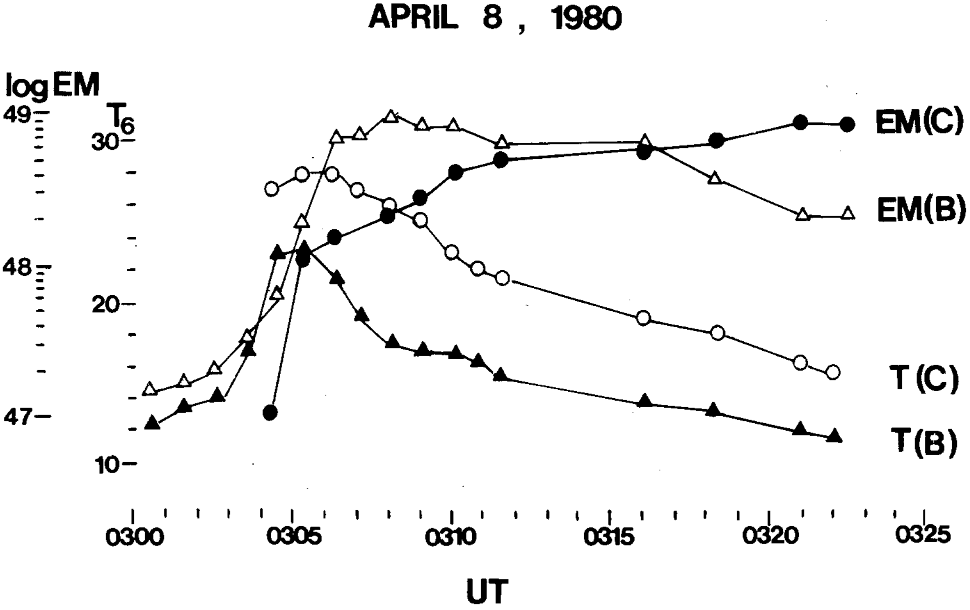

Fig. 5. Emission measure and temperature (in millions of degrees) of the different features in the April 8 flare. Before 03 : 04 UT the **B** curves mainly show the physical parameters characterizing feature **A**, but we omitted this discrimination in order to simplify the figure.

Feature **C** shows a very interesting behavior, being partically invisible to the HXIS before the impulsive burst, it appears shortly after its start showing a steep increase in EM and a rather high temperature. During the first minute of the brightness increase we derive an emission measure growth rate $d(EM)/dt \approx 2 \times 10^{46}\ \mathrm{cm}^{-3}\ \mathrm{s}^{-1}$, slowly decreasing thereafter until the total EM reaches a maximum at around 03^h20^m. We take these observations as a strong evidence that feature **C** is a loop system structure which is suddenly energized by interconnection with features **A** and **B**, also independent loop systems.

It should also be noted the relatively high temperature derived from the soft X-ray output (3.5–11.5 keV) of feature **C** (for discussions on how these temperatures are obtained we refer to van Beek *et al.*, 1981; Machado *et al.*, 1982). Although absolute values may be subject to errors, the differences between the temperatures of features **B** and **C** are accurate, and we take it as an evidence that a high energy electron population was injected into **C** at the time of the impulsive burst (see also a similar discussion by de Jager *et al.*, 1982). It is possible that high energy electrons ($E > 16$ keV) are injected into **C** but HXIS is unable to see their thin-target contribution to the hard X-ray spectrum. We have noted before that footpoint structures were barely visible in **B** at the time of the impulsive components, and allowing for the fact that a thick-target process is more efficient than thin-target, it is clear that for the low densities in structure **C** the hard X-ray output should be very weak. We shall return to this point when discussing the April 13 flares.

A fourth structure in the soft X-rays was observed by the HXIS late in the event. Figure 6 shows a coarse field of view image obtained at 04^h01^m UT during the SMM orbit following that of the start of the flare. The large structure, which we label **D**, overlays the whole active region complex going from the leading to the trailing spots. We also show for reference the corresponding image in the fine field of view. This feature, as it will aso be shown in the April 7 and 10 flare cases, is obviously a large loop system interconnecting leading and trailing parts of opposite polarity regions.

We thus conclude that four distinct magnetic structures, as sketched in Figure 7, took part in the flare. Potential field calculations based on the MSFC data for April 8 show these four structures, as demonstrated by Chen *et al.* (1982). The initial flare brightening and impulsive phenomena were concentrated in the region of highest shear in the

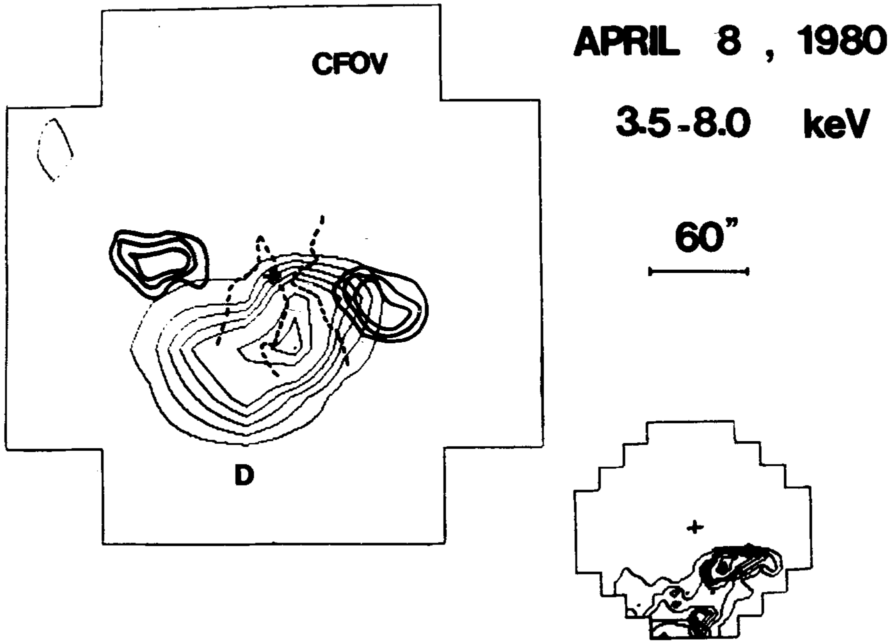

Fig. 6. Large soft X-ray structure seen by the HXIS at 04 : 02 UT in its coarse field of view (CFOV) under 32″ resolution. The corresponding fine field of view image is shown for comparison (cf. Figure 2), both fields have a common center.

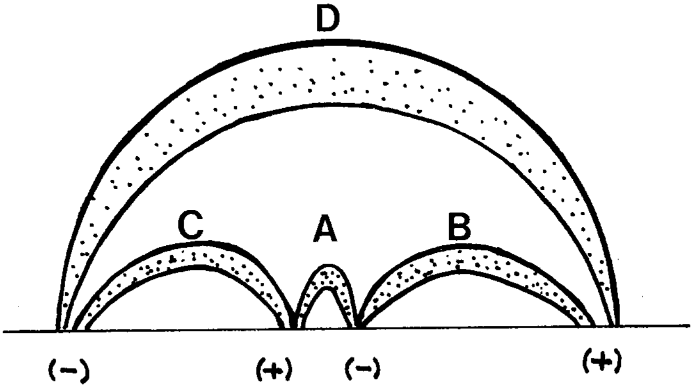

Fig. 7. Sketch describing the inferred location of the four X-ray structures with respect to the field configuration.

magnetic configuration, namely **A** and **B**, while **C** does seem only to be energized by its interaction with these two structures. The properties of region **D** will be discussed in Section 4.2.2.

4.2. THE APRIL 7 FLARES

Two flares occured within a four hour interval on April 7. Only the first, at 00^h51^m UT, was observed by the SMM from its beginning, but the second (starting in Hα at 05^h18^m) gives us the opportunity to study the late phases of its development in great detail. The two flares showed strinkingly similar spatial characteristics in the soft X-rays.

4.2.1. *The* 00^h51^m *Event*

A preliminary description of this flare has been given by Hoyng *et al.* (1981b). Figure 8 shows the temporal evolution of the spatial distribution of the emission in the HXIS soft and hard X-ray bands. As noted by Hoyng *et al.* (1981b), two emission features develop during the flare, bridging, as in the April 8 event, regions of opposite polarity between leader, trailer and the bipolar region (patches **B** and **C** in Figure 8).

The site of the initial flare brightening is masked in the contours of Figure 8a by the fact that feature **B** was already bright at the start of the event. Figure 9 shows the soft X-ray light curves of the individual features, together with the 16.0 to 30.0 keV emission curve of the total flare area, as recorded by the HXIS high energy monitor (HEM). From the soft X-ray light curves we see that the emission in **B** was decaying at the start of the observations, most likely showing the late cooling phase of a previous flare at 23^h10^m UT on April 6. Following the start of the 00^h51^m flare this decay stopped momentarily, as an evidence of new energy input into the flaring loop structures. The decay resumed again shortly after 01^h10^m, in coincidence with the start of the decline of **C**.

Although not clearly apparent from inspection of Figure 8, we find again in this flare the initial brightening related to point **A**, above the bipolar region (see Hoyng *et al.*, 1981b, for details on the alignment). Emission in the higher energies is rather diffuse and

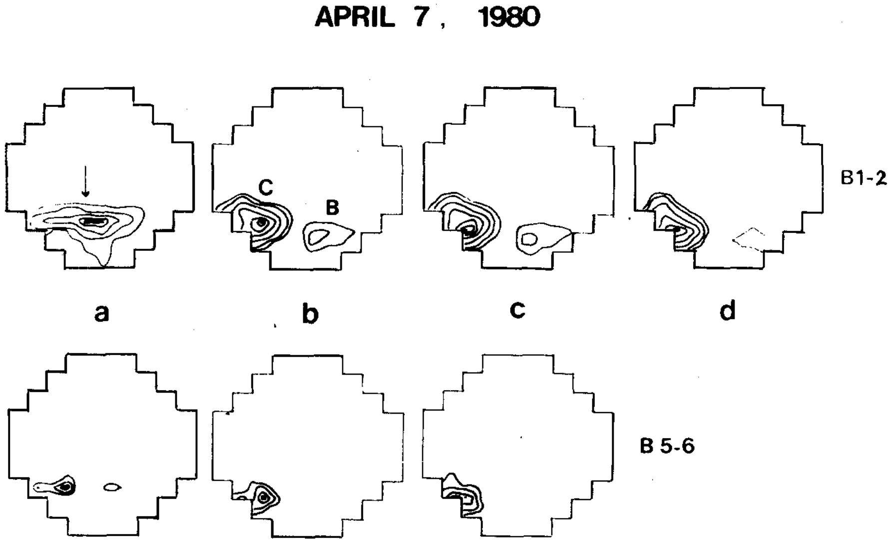

Fig. 8. Temporal evolution of the soft (B1–2: 3.5 to 8.0 keV) and hard (B5–6: 16.0 to 30.0 keV) structures in the April 7, 01 UT flare. The location of the intermediate bipolar region is shown by an arrow. Note that in (a) the emission tends to be concentrated there, although considerable pre-flare brightness was seen in **B**. The images correspond to: (a) 00 : 50 : 40 UT, (b) 00 : 52 : 47 UT, (c) 01 : 07 : 23 UT, and (d) 01 : 28 : 07 UT when no significant harder emission was detected. Contour levels are the same as in the previous sets.

weak at this time (coincident with the first, impulsive, peak in the HEM records of Figure 9), and no conclusions can be drawn from the images.

As shown by Hoyng *et al.* (1981b), the two features **B** and **C** separated. Only **C** showed 16.0 to 30.0 keV emission, while the spectrum of **B** was very soft. Through the development of the long enduring gradual burst as seen in the HEM light curve, **C** showed as S–E motion both in soft and hard X-rays. The locus of maximum emission in the harder X-rays moved ahead of the soft's by about 8″ (cf. Figure 8a, c). Interpreting these observations as the signature of a growing loop system, we find that the high energy emission consistently originated in structures overlying the softer, cooler, loops.

Two alternatives can be put forward to explain these observations, the emission could be due to thermal or thin-target processes. In the first case, using the same approach as in the Machado *et al.* (1982) analysis (see also Section 4.1), a two temperature fit of the flare X-ray emission can be performed. In Table II we give the results obtained for three times during the flare development. It should be noted that after $01^{h}07^{m}$ UT the count rates in the high-energy bands are too low for a meaningful analysis to be made. The softer X-ray patch **B** *never* shows significant count rate in the HXIS high energy bands, although it is clearly re-energized at the start of the event, as discussed above (see Figure 9).

The analysis shows that while the overall temperature of the soft plasma decayed, and its emission measure rised, both the temperature and emission measure of the hot

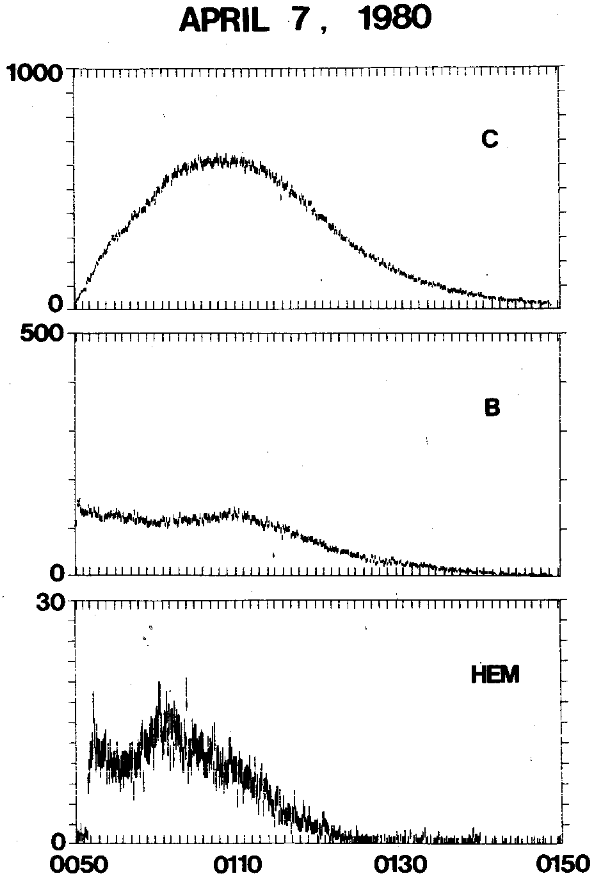

Fig. 9. Soft X-ray (3.5 to 8.0 keV) light curves of the individual features in the 01 UT event. Note the considerable pre-flare brightness of **B** and the change in the slope of its decaying trend. The HEM record corresponds to 16.0 to 30.0 keV emission, the abrupt jump at approximately 00 : 52 UT is partly due to a change in the instrumental mode of operation, but the peak is real.

components remained fairly constant. One should bear in mind, however, that since only one of the two HXIS microprocessors worked on April 7, data gathering occupied half of the time (the other half was spent in data transmission and the switch occurred every 4.5 s), therefore a $\Delta t = 36$ s spans 72 s of real time. The conductive cooling time, τ_c, of a 6×10^7 K region with emission measure $EM \approx 10^{46}$ cm^{-3} and length of the order of one to two HXIS pixels (8″ to 16″) can be computed from its saturated heat flux to be of the order of one to two seconds (see e.g., Machado *et al.*, 1982). Even if anomalous processes further limit the heat flux (see e.g., Smith and Lilliequist, 1979), we still find that $\tau_c \lesssim 10$ s. Therefore it is clear that the high temperature component parameters of Table II could be smoothed values over the heating and cooling phases of hot regions. Both higher and lower temperature components may be present over the integration periods, and the parameters are obtained through the folding of their X-ray emission and the HXIS efficiency.

TABLE II

Temperature and emission measures, April 7, 1980

t	Δt (s)	Feature **C**				Feature **B**	
		Low-T	EM	High-T	EM	T	EM
$00^h52^m40^s$	44	2.2×10^7	3.8×10^{48}	6×10^7	1.7×10^{46}	1.8×10^7	1.3×10^{48}
$00^h58^m30^s$	36	2.0×10^7	8.5×10^{48}	5.7×10^7	3.3×10^{46}	1.4×10^7	1.9×10^{48}
$01^h03^m23^s$	36	1.9×10^7	1.4×10^{49}	6.0×10^7	1.7×10^{46}	1.6×10^7	1.5×10^{48}

t = mean time within the integration interval.
Δt = integration time.
Low-T and T = estimated from count rates in bands 1, 2, and 3.
High-T = best-fit value of high temperature component needed to explain high counting rates in the 16 to 30 keV range (bands 5 and 6).

An alternate possibility, which could also in principle explain the HXIS observations, would be to assume that during the hard X-ray impulsive peak energetic electrons are injected and trapped in the magnetic structure defining feature **C**. For these $E \leq 30.0$ keV electrons to be able to exist within the trap for a period of several minutes, a rather low density has to be postulated ($n < 10^9$ cm^{-3}), unless they are continuously reaccelerated. If either of such conditions was realized, the high energy emission shift could be explained by increased efficiency in the production of hard X-ray photons within the trap, due to a gradual density enhancement by evaporated chromospheric material within progressively higher loop structures. It is however unclear why the brightest emission would preferentially be located within the loop structures and not at their feet, since density enhancements should start by an inflow of material from the chromosphere.

It should be noted that, again in this flare, the hard X-ray component originates from within the regions of highest shear in the field configuration. Throughout April 6 and the early hours of April 7, the MSFC magnetograms show highly sheared fields within the intermediate bipolar group and also in the region between this structure and the trailing spot. It is also within this time interval that not only the bipolar region migrated but also the trailing spot showed eastward motion (Krall *et al.*, 1982).

4.2.2. *The* 05^h18^m *Event*

The start and impulsive phases of this flare occurred during SMM orbital night. When the observations started at 05^h37^m, two soft X-ray features were clearly defined. Of these, again the eastern, connecting the bipolar region and the trailer, showed the brighter and longer lived hard X-ray component. Figure 10 shows the temporal evolution of the 3.5 to 8.0 keV and 16.0 to 30.0 keV emission for as long as they show significant count rates. The shift in the location of the two features within the field of view, as observed at 05^h43^m, is due to a spacecraft motion. Morphologically this flare is homologous to its predecessor, although it is twice as bright in soft X-ray intensity.

The most interesting aspect of the HXIS observations of this flare is related to the

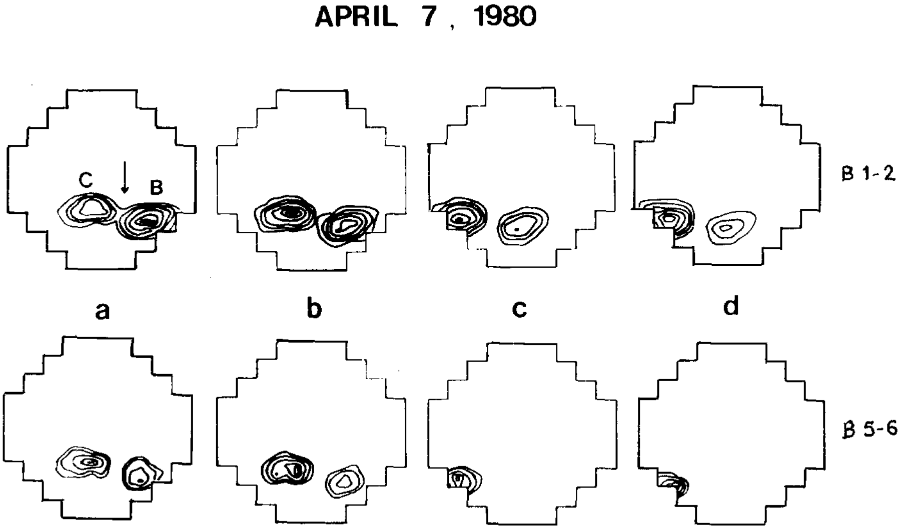

Fig. 10. Temporal sequence of soft and hard X-ray emission contours in the 05 UT event. The shift across the field of view in (c) is due to a spacecraft pointing change. Note here, as well as in Figure 8, that the loci of maximum emission in the two records are not cospatial, and that the harder emission moves ahead of the softer. The images correspond to: (a) 05 : 37 : 27 UT, (b) 05 : 39 : 37 UT, (c) 05 : 43 : 18 UT. The arrow again shows the location of the intermediate bipole.

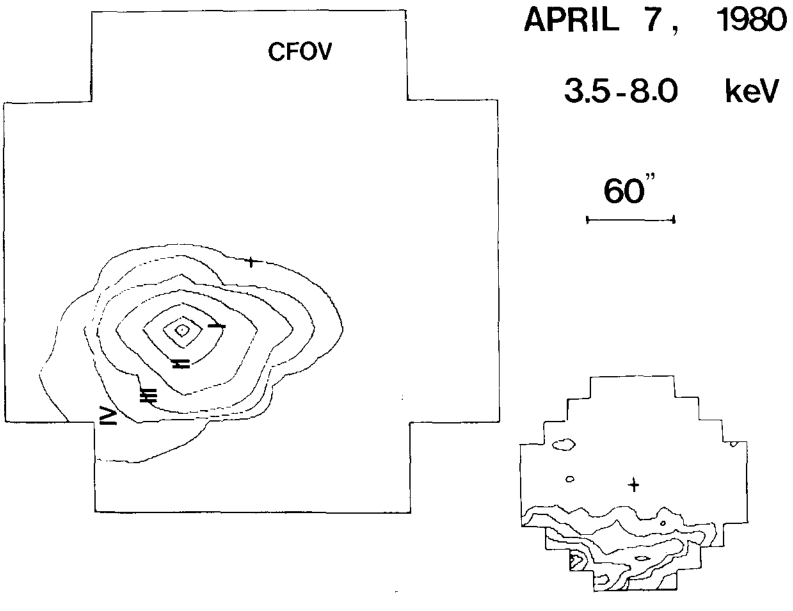

Fig. 11. Large soft X-ray structure seen in association with the 05 UT event. The contour levels correspond to 2, 5, 10, 25, 50, 75, 90, and 99% of the maximum. The four regions discussed in the text are noted, being 64" long in the E–W direction (in the sense in which the roman numerals can be read) and 32" wide (i.e., one HXIS CFOV pixel). The noise level is below 1%.

'post-flare' phase. Figure 11 shows a coarse field of view image obtained at 06^h17^m UT, which shows, as in the April 8 case, a large soft X-ray feature overlying the whole active region complex. Much of the post-flare coverage was spent by the HXIS looking at the Sun in its quiet mode, so that full coverage of the field of view is available (cf. Section 2) allowing us to study the evolution of the soft X-ray feature in detail.

We define four regions within the extended feature, as labeled **I** to **IV** in Figure 11, and we study the temporal evolution of count rate ratios in the HXIS low energy bands 1, 2, and 3. Except for regions **I** and **II**, the count rates in band 3 are too low after 06^h12^m to obtain meaningful estimates of temperatures and emission measures using ratios that involve this band. Table III shows the temperatures obtained from the B1/B2 ratios throughout the observing period. Although individual absolute values may have errors, differences between individual regions are meaningful, well above one-sigma fluctuations (ratios are obtained with an accuracy of ± 0.2 to ± 0.4 in regions **I** to **III**).

TABLE III

Temperatures of the soft X-ray cloud derived from bands 1 and 2 ratios

t	Δt (s)	Region **I** (B1/B2)[a]	Region **II**	Region **III**	Region **IV**
$06^h08^m56^s$	90.0	7.7×10^6 (2.5)	8.5×10^6 (1.7)	8.7×10^6 (1.5)	9.0×10^6 (1.4)
$06^h12^m01^s$	90.0	7.7×10^6 (2.5)	8.3×10^6 (1.8)	8.3×10^6 (1.9)	9.4×10^6 (1.2)
$06^h15^m05^s$	90.0	7.6×10^6 (2.9)	8.2×10^6 (2.0)	8.3×10^6 (1.9)	9.7×10^6 (1.1)
$06^h18^m10^s$	90.0	7.4×10^6 (3.5)	7.7×10^6 (2.4)	8.4×10^6 (1.8)	9.0×10^6 (1.4)
$06^h21^m14^s$	90.0	7.4×10^6 (3.4)	7.5×10^6 (2.9)	8.3×10^6 (1.9)	8.5×10^6 (1.7)
$06^h24^m18^s$	90.0	7.3×10^6 (3.6)	7.6×10^6 (2.7)	8.2×10^6 (2.0)	8.5×10^6 (1.7)

[a] (B1/B2): Measured ratio between counts in the HXIS bands 1 and 2.

Thus, Table III shows a consistent trend of temperature increase with height within the large feature, which can be interpreted as a large loop system connecting leading and trailing portions of the active region.

We select region **II** for further study, because it shows significant count rates in all three bands and is not as close to the original flare site as **I**, where we can expect some influence due to the low lying flare loops in the two patches.

TABLE IV

Emission measures in region **II**

t	EM(B1/B2)	T(B2/B3)	EM(B2/B3)
$6^h08^m56^s$	4.7×10^{48}		
$6^h10^m11^s$		18.6×10^6	2.5×10^{47}
$6^h12^m01^s$	4.3×10^{48}		
$6^h15^m05^s$		17.5×10^6	1.5×10^{47}
$6^h18^m10^s$	4.2×10^{48}	16.0×10^6	1.1×10^{47}
$6^h24^m18^s$	3.0×10^{48}		

(B1/B2) etc. define the band ratios from which the physical parameters were deduced.

Table IV shows the emission measures obtained from the B1/B2 counts and the temperature and emission measures derived from B2/B3 ratios obtained through longer (≈ 120 s) integration periods needed to improve count statistics in B3. Consistently larger temperatures are found when including band 3, indicating the possible existence of inhomogeneous structures within the large loop system.

The temperature decay rates can be estimated from the two sets of measurements to be

$$\mathrm{d}T/\mathrm{d}t = -1.4 \times 10^3 \ \mathrm{K\,s^{-1}} \tag{1}$$

from the B1/B2 ratio estimates and

$$\mathrm{d}T/\mathrm{d}t = -5.9 \times 10^3 \ \mathrm{K\,s^{-1}} \tag{2}$$

from B2/B3.

The length of the large loops can be estimated as $L \gtrsim 9 \times 10^9$ cm, and a maximum width can be assumed to be $\approx 30''$, so that the volume of region **II** is (for a tube a constant radius $R \lesssim 15''$) $V \leq 3.3 \times 10^{28}$ cm^3. This value leads to a lower limit in the mean density $n_{\min} \approx 10^{10}$ cm^{-3} (from the B1/B2 values) and $n_{\min} \approx 3 \times 10^9$ cm^{-3} from B2/B3.

The relationship between radiative and conductive timescales is given by

$$\tau_{\mathrm{rad}}/\tau_{\mathrm{cond}} \simeq \frac{3kT^{7/2}}{3 \times 10^{-10} n^2 l^2 \Phi(T)}\,, \tag{3}$$

where $\Phi(T)$ is the radiative loss function (see e.g., Raymond *et al.*, 1976) and l is a characteristic length scale which we take as $L/2$. For $10^7\ \mathrm{K} \leq T \leq 2 \times 10^7$ K, $\Phi(T) \approx 2.2 \times 10^{-23}$, so that with $l^2 \simeq 2 \times 10^{19}$ cm^2 we obtain

$$\tau_{\mathrm{rad}}/\tau_{\mathrm{cond}} \approx \frac{2.7 \times 10^{22}}{n^2} \quad \text{for} \quad T \approx 1.5 \times 10^7\ \mathrm{K} \tag{4}$$

and

$$\tau_{\mathrm{rad}}/\tau_{\mathrm{cond}} \approx \frac{6.6 \times 10^{21}}{n^2} \quad \text{for} \quad T \approx 10^7\ \mathrm{K}\,. \tag{5}$$

This shows that at least the initial cooling stage of such loops should be governed by heat conduction, unless we asume a small filling factor within the coarse field of view pixels.

The rate of energy decay due to heat conduction losses is given by

$$\mathrm{d}E/\mathrm{d}t = \frac{\mathrm{d}(3nkTV)}{\mathrm{d}t} = -1.1 \times 10^{-6}\, T^{7/2} A/l \ \mathrm{erg\,s^{-1}}\,, \tag{7}$$

where A is the crosssection of the loops. Assuming V and n constant and approximately equal to the values given above, we find

$$\mathrm{d}T/\mathrm{d}t = -4.6 \times 10^{-15} A\,. \tag{8}$$

So, if

$$1.4 \times 10^3 \leq |\mathrm{d}T/\mathrm{d}t| \leq 5.9 \times 10^3 \text{ K s}^{-1} \tag{9}$$

as measured, we obtain

$$3 \times 10^{17} \leq A \leq 1.2 \times 10^{18} \text{ cm}^2 .$$

The upper limit of A is in rather good agreement with the value assumed, and implies $V \approx 10^{28}$ cm^3. If A would be as small as 3×10^{17} cm^2, then $V = 3 \times 10^{27}$ cm^{-3} and still $n \approx 3.6 \times 10^{10}$ cm^{-3} as an absolute upper limit, so that conduction remains as the dominant cooling mechanism.

We would like to point out here that the results obtained in this section are in agreement with the physical parameters derived from data sets related to other flares in this region. We chose to discuss these in detail because of the good temporal coverage.

4.3. April 10, 09$^{\mathrm{h}}$14$^{\mathrm{m}}$ UT

The HXIS observations concerning this flare have been discussed in detail by Machado *et al.* (1982; see also Hoyng *et al.*, 1981b).

The flare occurred in the leader portion of the active region, between the bipolar region and the leader spot, showing only a weak emission region extending towards the trailer. There are some indications (Machado *et al.*, 1982) that the initial flare brightening occurred in a small structure closely localized around the intermediate bipole, but during the impulsive phase, two well defined high energy footpoints were observed at the edges of what would be the equivalent of feature **B** in the April 8 flare (see Machado *et al.*, 1982; Duijveman *et al.*, 1982). Thus, again in this flare the hard component of the X-ray emission originated from within a loop structure connecting the bipolar region and the leader.

Post-flare soft X-ray images, although scarce in terms of full field of view coverage, show once more the large structure overlying the active region complex.

The characteristics of the magnetic field configuration are more difficult to determine at this time, due to foreshortening effects. We note however that, as stated by Krall *et al.* (1982), no significant spot motions were seen in this period.

4.4. The April 13 flares

The view at the limb gives us a better opportunity to study the height structure of soft and hard X-ray emission. No evidence of large post-flare structures were found this day, but sympathetic flare activity was seen between AR 2372 and AR 2370 located towards the N–E. Connecting soft X-ray structures were observed between the two regions.

Of the two flares listed in Table I only the one at 04$^{\mathrm{h}}$05$^{\mathrm{m}}$ UT was observed from its beginning.

Two clearly defined soft X-ray structures can be seen in these events. Figure 12 shows the soft X-ray evolution of the 04$^{\mathrm{h}}$ flare, we note that the initial brightening occurs in a small kernel (**K**), while shortly thereafter a second, much larger (**T**) structure begins to develop. Figure 13 shows the soft X-ray light curves for these two structures, together

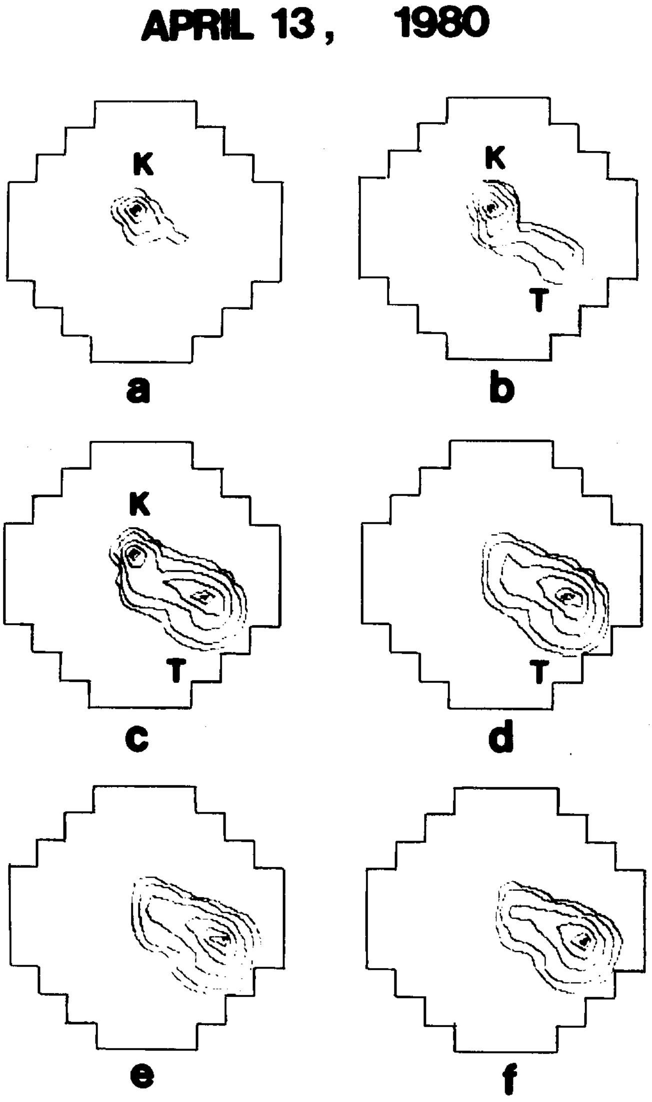

Fig. 12. Evolution of the soft (3.5 to 8.0 keV) emission in the April 13, 1980 flare. Note the faster decay of the X-ray kernel **K**, as compared with the large feature **T**. The contours correspond to: (a) 04 : 04 : 29 UT, (b) 04 : 06 : 03 UT, (c) 04 : 13 : 39 UT, (d) 04 : 17 : 29 UT, (e) 04 : 25 : 20 UT, and (f) 04 : 31 : 39 UT. The hard X-ray burst was recorded at 04 : 05 : 20 UT (cf. Figure 13), so that (a) shows pre-burst brightening of **K**.

with the 22.0 to 30.0 keV record of the high energy monitor. We note that a weak, impulsive, short lived hard X-ray burst occurs during the rising phase of both **K** and **T** structures, at lower energies.

Examination of the HXIS 16.0 to 30.0 keV images (Figure 14) integrated through the duration of the impulsive burst shows the striking fact that the bulk of the emission is concentrated at the boundary between **K** and **T**, extending into structure **T** which is barely visible in soft X-rays at this time.

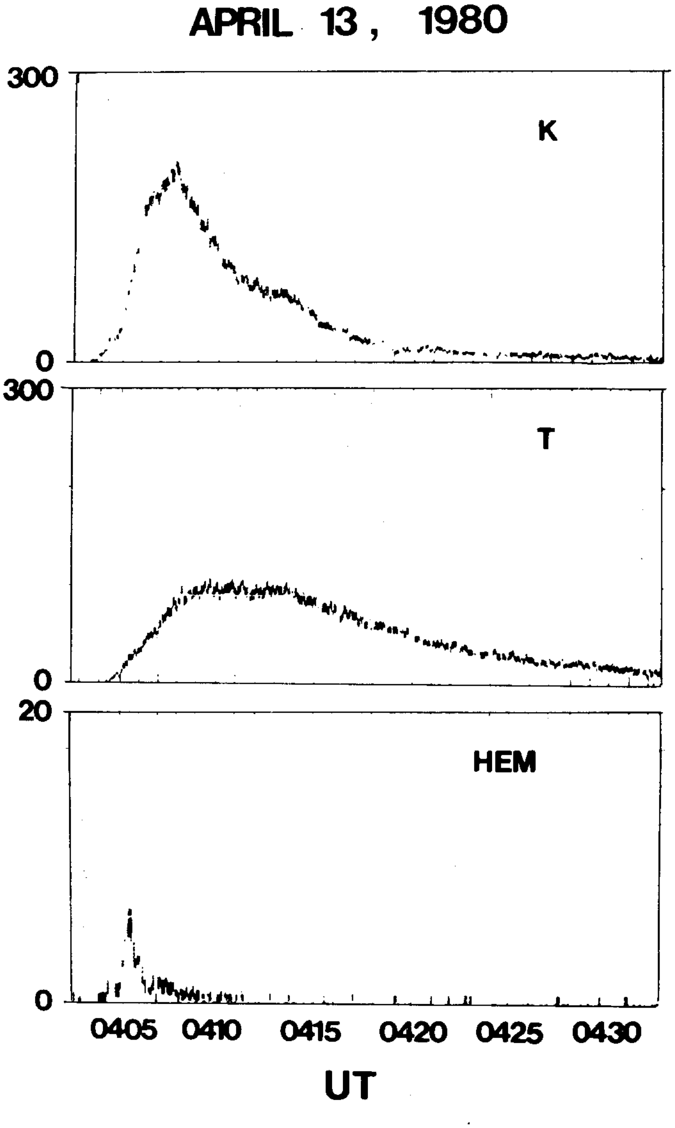

Fig. 13. Soft (3.5 to 5.5 keV) X-ray light curves of features **K** and **T** in the April 13 flare, and 22.0 to 30.0 keV records of the High Energy Monitor indicating the impulsive hard X-ray burst. Note the fast decay of the **K** emission, the shoulder in its light curve at around 04 : 12 UT is due to spatial superposition of the two structures in the field of view pixels. The emission of **K** has been integrated over six $(8'')^2$ pixels and that of **T** over 8 pixels.

If we make the hypothesis that the hard X-ray burst is due to bremsstrahlung emission by particles accelerated at the region of interaction between the two structures, and we further assume that the emission along this boundary is due to a thin-target process (see e.g., Kane and Anderson, 1970) we can compute the electron emission measure from

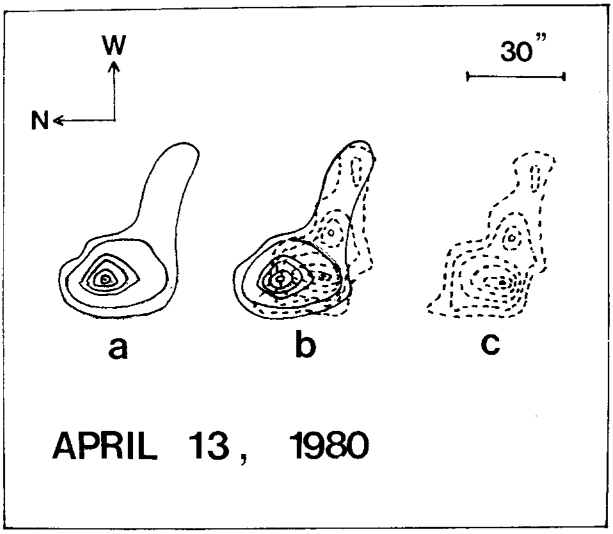

Fig. 14. Soft (a, 3.5 to 8.0 keV) and hard (c, 16.0 to 30.0 keV) X-ray emission contours obtained from the HXIS images integrated over 25 s at the peak of the hard X-ray burst. Figure 14b shows the superposition of the two images. See text for details.

the thin-target formula

$$I(E) = 1.16 \times 10^{-42} \frac{\Gamma(\gamma)}{(\gamma - 1)^2 \Gamma(\gamma - \frac{1}{2})} n_e N(E) E^{-1/2}, \tag{10}$$

where $I(E)$ is the observed intensity at energy E, and γ is the photon spectral index. The observed intensity at 20 keV is $I(20) \approx 10$ photons cm^{-2} s^{-1} keV^{-1} integrated along the boundary over an area of 3 by 1 pixels extending from the southern part of **K** into **T**. The spectral index $\gamma \approx 5$ as deduced from the ratio between bands 5 and 6 is in agreement with the one deduced from the HXRBS data (Smith and Orwig, 1982. Note that in this paper the emission was treated as produced from within a closed, compact loop structure, which is clearly incorrect). We thus obtain $n_e N(20) \approx 5 \times 10^{44}$ and assuming that the power-law distribution of electrons extends down to 10 keV (the HXIS band 4, covering the 11.5 to 16.0 keV range shows similar behavior) we get

$$n_e N(10 \text{ keV}) \approx 10^{46} \text{ cm}^{-3} .$$

Considering that ≥ 10 keV electrons move at ≥ 0.2 of the speed of light and that the length to be traversed is $\approx 1.7 \times 10^9$ cm, if we assume that $10^{10} \leq n_e < 10^{11}$ cm^{-3} (for $n_e \gtrsim 10^{11}$ cm^{-3} the 10 keV electrons would be stopped within one HXIS pixel) we obtain that $\approx 5 \times 10^{35}$ electrons s^{-1} are accelerated to energies $E \geq 10$ keV. This number is most likely an upper limit, since we might expect to have a thick target contribution at the feet of the loops defining the kernel **K**. The total energy content in the electrons accelerated during the hard X-ray burst (FWHM $\simeq 30$ s) is then $\leq 5 \times 10^{30}$ erg, a fraction of which is injected into structure **T**.

TABLE V

April 13, temperatures and emission measures

Time	T(K)	EM(K)	T(T)	EM(T)
$4^h05^m06^s$	21×10^6	7.0×10^{47}	24×10^6	2.5×10^{47}
$4^h05^m38^s$	22×10^6	1.3×10^{48}	26×10^6	4.4×10^{47}
$4^h06^m10^s$	21×10^6	2.1×10^{48}	26×10^6	6.3×10^{47}
$4^h06^m49^s$	21×10^6	2.4×10^{48}	23×10^6	1.0×10^{48}
$4^h07^m21^s$	21×10^6	2.5×10^{48}	24×10^6	1.2×10^{48}
$4^h07^m53^s$	19×10^6	3.0×10^{48}	23×10^6	1.4×10^{48}
$4^h08^m42^s$	18×10^6	3.2×10^{48}	22×10^6	1.6×10^{48}
$4^h08^m59^s$	18×10^6	3.0×10^{48}	20×10^6	2.0×10^{48}
$4^h09^m30^s$	17×10^6	2.9×10^{48}	21×10^6	1.9×10^{48}
$4^h10^m03^s$	17×10^6	2.8×10^{48}	21×10^6	1.9×10^{48}
$4^h10^m33^s$	17×10^6	2.4×10^{48}	19×10^6	2.3×10^{48}
$4^h11^m07^s$	16×10^6	2.4×10^{48}	19×10^6	2.0×10^{48}
$4^h11^m39^s$	17×10^6	2.0×10^{48}	18×10^6	2.0×10^{48}

Table V shows the evolution of T and EM in structures **K** and **T** as a function of time. We note that we confirm the previous result (cf. Section 4.1., van Beek *et al.*, 1981; de Jager *et al.*, 1983) that the large structure is hotter than the small kernel.

Assuming a volume $V \simeq 7 \times 10^{27}$ cm^3 for the large region (3 by 3 by 4 pixels) and uniform filling, we can calculate its thermal energy content from

$$E_{\text{th}} = \frac{3kEMT}{n} \tag{11}$$

and from the values listed in Table V we obtain $E_{\text{th}} \approx 1.3 \times 10^{30}$ erg at around 04^h09^m UT, remaining approximately constant, within the observational uncertainties, for a period of one minute. This value of E_{th} is most likely an upper limit, due to our assumption of uniformity in the volume. Therefore, we find that the energy content of the accelerated electron population can account for E_{th}, suggesting that structure **T** is just energized by these accelerated particles. We find that, within the observational accuracy, the hotter structure **T** shows uniform temperature at all heights, and there is no evidence of localized energy release within it. The fact that we observe the hard X-ray emission concentrated within the boundary between **K** and **T** is most likely related to higher densities within that region, and thus increased thin-target efficiency, The average density of structure **T** at the time of the hard X-ray burst would be $n < 10^{10}$ cm^{-3} (assuming again that $V_T = 7 \times 10^{27}$). The density of **K**, which *does show* a hard X-ray emission component, can be estimated as $n \approx 5 \times 10^{10}$ cm^{-3}, assuming a volume $V_K \approx 4 \times 10^{26}$ cm^3.

A second flare, with similar spatial characteristics, stated at 08^h34^m UT. Its impulsive phase occurred during SMM night. At 08^h43^m, when the HXIS observations started, both structures **K** and **T** where clearly visible, with the kernel already decaying. It is interesting to note that if we believe that both flares were due to the interaction between the structures, such a phenomenon occurred with similar spatial characteristics and intensities (the first flare was only a factor 1.7 times brighter in soft X-rays) within a period of 4 hr.

Good radio spectra are available for this second event showing a large group of type III radio bursts up to metric wavelengths.

5. Related Hα and Radio Observations

High quality Hα filtergrams are rather scarce for the flares discussed in this paper. In Figure 15 we show an Hα picture taken at $00^{\mathrm{h}}52^{\mathrm{m}}$ UT on April 7, showing a four-ribbon type of structure. The location of these Hα patches coincides with the feet of the soft X-ray loops of patches **B** and **C** in Figure 8.

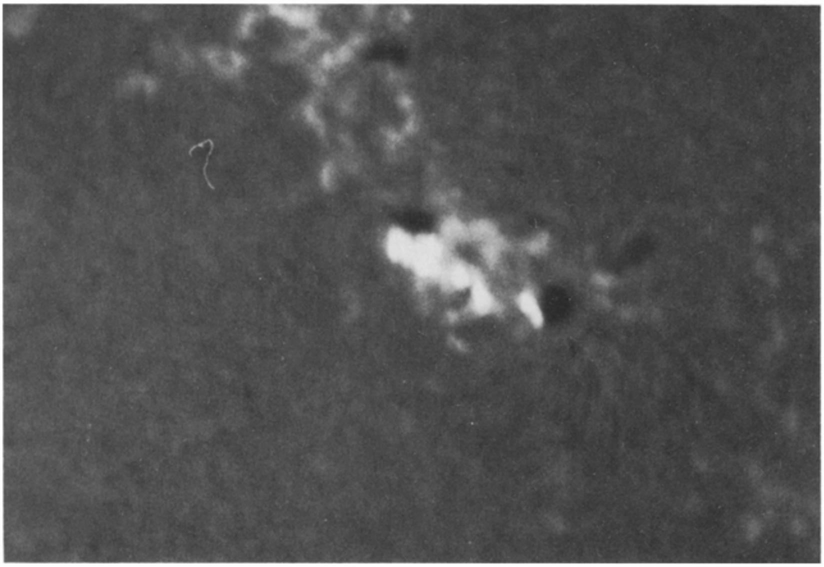

Fig. 15. Hα picture of the April 7 flare obtained at 00 : 55 : 32 UT. Note the clearly separated bright ribbons indicating the feet of the different magnetic structures. (Courtesy of H. Zirin, Big Bear Solar Observatory.)

Similar behavior was observed in flares occurring on April 6 while the SMM was not pointed at the region (Falciani, 1981). After April 7, much of the strongest activity in Hα shifted towards the leader portion of the active region, in agreement with the behavior observed in the X-rays.

Post flare Hα observations of a flare at $17^{\mathrm{h}}55^{\mathrm{m}}$ UT on April 6 showed a big absorption arcade connecting the leader and trailing portions of the region, with filamentary structures of few arc seconds in diameter (Falciani, 1981). This structure might be related, as we discuss in the next section, to the cooling of the large loop system observed in the other flares.

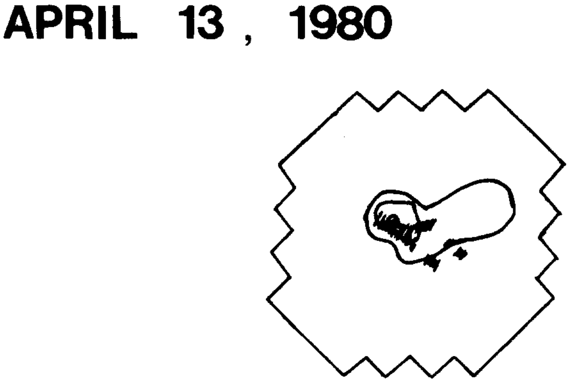

Fig. 16. Overlay of Hα and X-ray structures in the April 13 flare. The Hα picture (courtesy of A. Bhatnagar, Udaipur Observatory) was obtained at 04 : 07 : 52 UT. Note in the sketch on the right that the brightest Hα emission is located at the site of the kernel **K**, but distant brightenings, presumably at the feet of the larger, **T** loops, are observed. The location of the surge-like feature coincides with that of the hard X-ray emission at the time of its impulsive burst (cf. Figure 14), within the accuracy of our alignment.

Hα observations of the April 13, 04^h05^m UT flare (Figure 16) show the development of a bright region at the site of the X-ray kernel **K**, a surge-like structure at its edge, and several weaker brightenings most likely associated with the feet of the magnetic structure defining **T** in the X-ray observations.

Figure 16 shows the overlay of the Hα and X-ray observations, in which we see that the Hα ejection approximately proceeds along the boundary between **K** and **T** i.e. the site of the most energetic phenomena. The same type of correlation, but with a UV transition zone line, has been reported by Poland *et al.* (1982).

Radio spectral observations (Table VI) show continuous noise storm activity associated with the flares from April 6 to 10. The location of these noise storms as seen at metric wavelengths corresponds, at higher altitudes, with that of the post flare large

TABLE VI

Radio emission associated with the AR 2372 flares

Date	
April 6 (all flares)	CONT, IV, V, I
April 7, 01 UT	IS, III NGB
April 7, 05 UT	CONT, IV – metric
April 8	III G, V
April 10	CONT, V, U-type bursts, III G
April 13, 08 UT	III G G (decimetric and metric)

Notes:

IS: intermitent but connected type I activity.

III NGB: intermitent type III activity with either smal groups or single bursts.

III G G: large group of type III bursts.

structures seen by the HXIS (Pick and Raoult, private communication). The fact that during the decay phase of the flare we observe in many cases intermitent enhancements at m-waves, possibly indicates that acceleration processes continued at high altitudes for a long period after the impulsive phase in the hard X-rays (see Klein *et al.*, 1983).

6. Discussion

In connection with solar flare theories, it was Sweet (1958, 1969) the first to describe the existence of independent loop systems separated by intersecting magnetic surfaces. The lines of intersection join pairs of neutral points and, when a neutral sheet forms, it is centered on this line. Syrovatskii (1973) described the separating line as a three-dimensional generalization of the well known X-type neutral line.

Lately, Baum and Bratenahl (1980) have considered a potential field configuration of four pointlike sunspot sources with a minus-plus-minus-plus configuration. They show the location and geometrical properties of the line of self-intersection of these sources, which they call the *separator.*

With the same terminology, and following the authors cited above, we can consider the separator as the most likely place of field reconnection and primary energy release within the active region. Let us consider the topological model of Figure 17, where we do not suggest a high symmetry in the magnetic sources, the separator being a neutral, zero line of longitudinal field (Syrovatskii, 1982). In Figure 17a, b the separator is shown by the solid line connecting two neutral points X_1 and X_2. The magnetic field component along the separator (B_l) is in general not null. N_l is the photospheric 'neutral line'.

The predictions of such a simple topological model are shown in Figure 18. Four different regions can be defined as follows:

(1) Region of magnetic reconnection, energy dissipation, heating and particle acceleration. Directions of magnetic reconnection are shown by arrows and determined by the sign of an electric field, induced along the separator, by changes of magnetic field sources on the photosphere and by magnetic shear relaxations.

(2) Magnetic raking and compression of the heated coronal plasma producing high temperature low X-ray loops which subsequently cool in short timescale.

(3) Cool dense loops over the photospheric neutral line (cf. Zirin *et al.*, 1981).

(4) Magnetic raking-up creates high temperature loops at large heights. These loops cool initially by heat conduction, but if compression becomes important they can develop a thermal instability and produce cool dense Hα loops high in the corona (see below).

It is clear that this is a simplified approach towards our understanding of the observed phenomena. Advantages and flaws of the topological approach are easily noticeable.

First of all we note that it naturally explains the fact that the initial brightening is located over the bipolar region. It does not however explain why the impulsive phenomena are concentrated towards one side (bipole and trailer on April 7 or bipole and leader on April 8 to 10), with in-situ energy release within such structures (the gradual phase in the hard X-rays). This however may be related to the magnetic shear

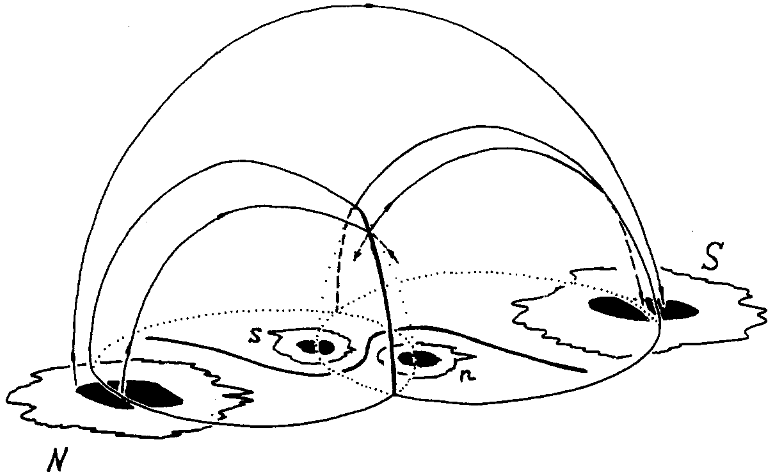

Fig. 17a. Topology of the field with intersecting flux systems in a region like AR 2372 (see text and Sweet, 1969).

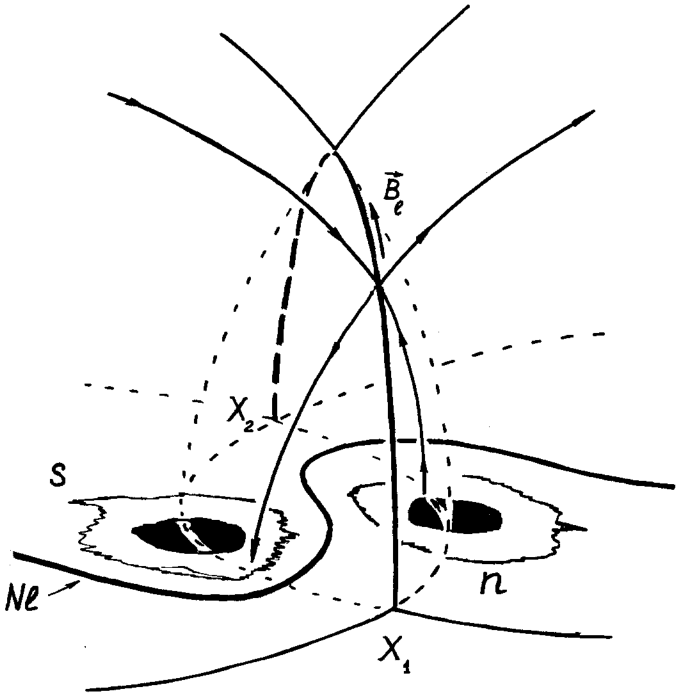

Fig. 17b. Blow-up of the central part of Figure 17a. The separator is shown by the line joining the two neutral points X_1 and X_2. N_l is the photospheric neutral line.

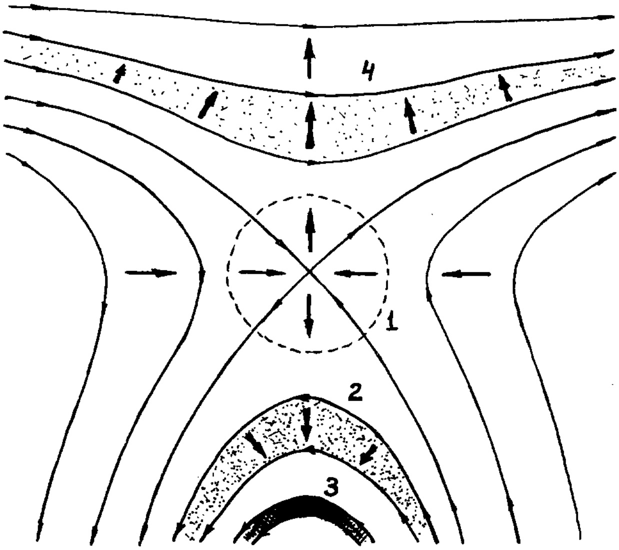

Fig. 18. Plasma dynamics predicted from the topological model of Figure 17. See text for details.

(i.e., currents) induced by the photospheric motions. Detailed analysis of such movements, also in terms of torsional shear, are essential for the whole discussion. We note that Krall *et al.* (1982) report that no spot motions were seen after April 7, but they do not study the possibility of seeing a velocity shear at the photospheric level. On the other hand, the formation of an electric double layer on the separator may be very important for understanding the impulsive phenomena (Baum and Bratenahl, 1982). Double layers create a preferential direction for electron acceleration by the electric field, so that the impulsive phenomena may have some asymmetry in the hard X-ray images, even in the case of a highly idealized model.

The production of the high altitude large features is also a natural consequence in the topological approach. A high temperature cloud is created in region 4 of Figure 18, this is the region of magnetic raking-up and compression, where the field has two distinct components (see Somov and Syrovatskii, 1974):

$$B = B_p + B_f\,, \tag{12}$$

where B_p is the potential and force-free part and B_f the non-potential component leading to compression.

The potential part of the magnetic field must be larger than B_{min} given by

$$B^2_{\text{min}}/8\pi = p_{\text{gas}}\,; \tag{13}$$

thus

$$B_{\text{min}} \approx 4\sqrt{\pi nkT} = 9 \times 10^{-8}\sqrt{nT} = 25\ \text{G}\,, \tag{14}$$

when one assumes $n \approx 10^{10}$ cm^{-3} and $T \approx 8 \times 10^6$ K as discussed in Section 4.2. This value of the magnetic field is rather large, but also subject to the uncertainties in the observational parameters.

We know from at least one observational case that elongated, thin, Hα absorption features were seen across the active region (Section 5). These are most likely due to a condensation mode of thermal instability (Field, 1965) induced by magnetic compression. We can then estimate very crudely the value of the non-potential part, B_f, of the magnetic field.

A thermal instability will start if the column number density, $N(\mathrm{cm}^{-2})$, along the loops exceeds the value (cf. Equation (3))

$$N_{\min} = \left(\frac{1.1 \times 10^{-6}\, T^{7/2}}{\Phi(T)}\right)^{1/2} \mathrm{cm}^{-2}\,. \tag{15}$$

Here we neglect a factor $(1 - \mathrm{d}\ln\Phi/\mathrm{d}\ln T)^{-1/2} \approx 1$ (see Equation (4.5) in Somov and Syrovatskii, 1976). With the above parameters, we find from (15) that

$$N_{\min} \approx 2.5 \times 10^{20}\,\mathrm{cm}^{-2}\,.$$

From the most likely parameters obtained in Section 4.2 we find that $N(\mathrm{loop}) \approx 9 \times 10^{19}\,\mathrm{cm}^{-2}$ so that no instability is likely, as already stated.

The condensation mode can start only after compression, when the density exceeds a critical value given by

$$n_{\mathrm{cr}}/n = N_{\min}/N \approx 2.7 \tag{16}$$

so that $n_{\mathrm{cr}} \approx 2.7 \times 10^{10}\,\mathrm{cm}^{-3}$.

The characteristic time scale of magnetic field changes within the raking-up region does not exceed the reconnection time scale, so that

$$\tau_B \approx \frac{L}{\alpha v_{\mathrm{A}}} \approx 10\sqrt{4\pi M}\, L\sqrt{n}/B_f\,, \tag{17}$$

where v_{A} is the Alfvén velocity and $\alpha < 1$ is a parameter which we assume to be 0.1 as an order of magnitude (Priest, 1981). It is clear that the estimate based on (17) is open to criticism, but it corresponds to the simplest approach which could hardly be improved without large complications of our qualitative model. Moreover, the only thing that is essential to our analysis is that the time τ_B must be shorter than the radiative cooling timescale, which is found to be $\tau_{\mathrm{rad}} \approx 3 \times 10^3$ s for a density $n \approx n_{\mathrm{cr}}$. We thus find from (17) that

$$\tau_B \lesssim \tau_{\mathrm{rad}} \quad \text{if} \quad B_f \gtrsim 0.5\ \mathrm{G} \tag{18}$$

which is the non-potential field component needed for compression. A comparison of the estimates (14) and (18) shows that the magnetic field configuration is mainly potential or force-free, as we tacitly suggested a priori.

The predicted density of the Hα structures are

$$n_{\mathrm{H}\alpha} \approx n_{\mathrm{cr}}(T/10^4\ \mathrm{K}) \approx 2 \times 10^{13}\,\mathrm{cm}^{-3} \tag{19}$$

and their width, with $n_{H\alpha}/n \approx 2 \times 10^3$, is

$$L(n/n_{H\alpha}) < d < L(n/n_{H\alpha})^{1/2}\,, \tag{20}$$

i.e.

$$4 \times 10^6 \text{ cm} < d < 2 \times 10^8 \text{ cm}\,,$$

in agreement with the observations that show arc-second structures. These values are of course very crude, since they strongly depend on the density and temperature of the cloud plasma at the start of the condensation.

Finally, we point out that the characteristics of the radio noise storms can be explained by a continuing slow reconnection process proceeding at high altitudes during the late phases of the flares.

The hard X-ray observations of the April 13 event can in principle be related to particle acceleration within a current sheet, as described by Somov and Syrovatskii (1975), Heyvaerts and Priest (1976), and Heyvaerts *et al.* (1977), or within an electric double layer, formed near the top of the separator (Baum and Bratenahl, 1982). It remains to be seen if the magnetic configuration and other observable parameters agree with the predictions of this model. To the latter point we should mention that Poland *et al.* (1982) have studied an event with characteristics similar to those of the April 13 flare, which occurred on June 29, 1980, and they found *impulsive brightenings* in the O V line λ 1371 Å (characteristic temperature of formation $T \approx 2.5 \times 10^5$ K) *above the limb* at the boundary between the two structures. This observational evidence again points to the existence of condensing high density plasma perhaps within a current sheet (see Priest, 1981, for a review).

Acknowledgements

Part of this work was done while two of us (MEM and BVS) were guest at the Space Research Laboratory in Utrecht; we would like to acknowledge the kind hospitality of its members.

We are most grateful to A. Boelee, A. Duijveman, P. Hoyng, and Z. Švestka of the Laboratory in Utrecht and J. B. Smith, Jr. of the Marshall Space Flight Center and NOAA for many helpful discussions. A. Bhatnagar, R. Falciani, A. Raoult, and H. Zirin provided ground-based data that helped in our understanding of the X-ray observations, and M. Galama (Utrecht) and M. C. de Frecha (San Miguel) gave excellent technical support.

The development and construction of the HXIS was made possible by the support given by the Dutch Ministry for Education and Science, through the Committee for Geophysics and Space Research of the Royal Dutch Academy of Arts and Sciences, and by the Science Research Council of the United Kingdom.

References

Baum, P. J. and Bratenahl, A.: 1980, *Solar Phys.* **67**, 245.

Baum, P. J. and Bratenahl, A.: 1982, in R. E. Lingenfelter, H. S. Hudson and D. M. Worrall (eds.), 'Gamma Ray Transients and Related Astrophysical Phenomena', *AIP Conf. Proc.* **77**, 433.

Cheng, C. C., Bruner, E. C., Tandberg-Hanssen, E., Woodgate, B. E., Shine, R. A., Kenny, P. J., Henze, W., and Poletto, G.: 1982, *Astrophys. J.* **253**, 353.

de Jager, C., Machado, M. E., Schadee, A., Strong, K. T., Švestka, Z., Woodgate, B. E., and van Tend, W.: 1983, *Solar Phys.* **84**, 205.

Duijveman, A., Hoyng, P., and Machado, M. E.: 1982, *Solar Phys.* **81**, 137.

Falciani, R.: 1981, Report to the Annecy SMY Workshop.

Field, G. B.: 1965, *Astrophys. J.* **142**, 531.

Heyvaerts, J. and Priest, E. R.: 1976, *Solar Phys.* **47**, 223.

Hoyng, P., Machado, M. E., Duijveman, A., and 21 co-authors: 1981a, *Astrophys. J. Letters* **244**, L153.

Hoyng, P., Duijveman, A., Machado, M. E., Rust, D. M., Švestka, Z., and 7 co-authors: 1981b, *Astrophys. J. Letters* **246**, L155.

Kane, S. R. and Anderson, K. A.: 1970, *Astrophys. J.* **162**, 1003.

Klein, L., Anderson, K. A., Pick, M., Trottet, G., Vilmer, N., and Kane, S. R.: 1983, *Solar Phys.* **84**, 295.

Krall, K. R., Smith, Jr., J. B., Hagyard, M. J., West, E. A., and Cumings, N. P.: 1982, *Solar Phys.* **79**, 59.

Lin, R. P., Schwartz, R. A., Pelling, R. M., and Hurley, K. C.: 1981, *Astrophys. J. Letters* **251**, L109.

Machado, M. E., Duijveman, A., and Dennis, B. R.: 1982, *Solar Phys.* **79**, 85.

Poland, A. I., Machado, M. E., Wolfson, C. J., Frost, K. J., Woodgate, B. E., Shine, R. A., Kenny, P. J., Cheng, C. C., Tandberg-Hanssen, E. A., Bruner, E. C., and Henze, W.: 1982, *Solar Phys.* **78**, 201.

Priest, E. R.: 1981, in E. R. Priest (ed.), *Solar Flare Magnetohydrodynamics*, Gordon and Breach.

Raymond, J. C., Cox, D. P., and Smith, B. W.: 1976, *Astrophys. J.* **204**, 290.

Smith, D. F. and Lilliequist, C. G.: 1979, *Astrophys. J.* **232**, 582.

Smith, D. F. and Orwig, L.: 1982, *Astrophys. J.* **258**, 367.

Somov, B. V. and Syrovatskii, S. I.: 1974, in *Neutral Sheets in Plasmas*, Proceedings (Trudy) of the P. N. Lebedev Phys. Inst. No. 74, Consultants Bureau, New York and London.

Somov, B. V. and Syrovatskii, S. I.: 1975, *Bull. Acad. Sci. USSR, Phys. Series* **39**, No. 2, 109, Allerton Press Inc., New York.

Somov, B. V. and Syrovatskii, S. I.: 1976, *Sov. Phys. Usp.* **19**, 813.

Sweet, P. A.: 1958, *Nuovo Cimento Suppl.* **8**, Ser. X, 188.

Sweet, P. A.: 1969, *Ann. Rev. Astron. Astrophys.* **7**, 149.

Syrovatskii, S. I.: 1973, *Vestnik AN SSSR* **3**, 31.

Syrovatskii, S. I.: 1982, *Solar Phys.* **76**, 3.

Syrovatskii, S. I. and Somov, B. V.: 1980, in M. Dryer and E. Tandberg-Hanssen (eds.), 'Solar and Interplanetary Dynamics', *IAU Symp.* **91**, 425.

van Beek, H. F., Hoyng, P., Lafleur, B., and Simnett, G. M.: 1980, *Solar Phys.* **65**, 39.

van Beek, H. F., de Jager, C., Fryer, R., Schadee, A., Švestka, Z., and 19 co-authors: 1981, *Astrophys. J. Letters* **244**, L157.

Woodgate, B. E., Tandberg-Hanssen, E. A., and 12 co-authors: 1980, *Solar Phys.* **65**, 73.

Zirin, H. Feldman, U., Doschek, G. A., and Kane, S. R.: 1981, *Astrophys. J.* **246**, 321.